MOLECULAR AND IONIZED HYDROGEN IN 30 DORADUS. I. IMAGING OBSERVATIONS

Sherry C. C. Yeh[1,2], Ernest R. Seaquist[2], Christopher D. Matzner[2], Eric W. Pellegrini[3]

ABSTRACT

We present the first fully calibrated H_2 1–0 S(1) image of the entire 30 Doradus nebula. The observations were conducted using the NOAO Extremely Wide-Field Infrared Imager on the CTIO 4-meter Blanco Telescope. Together with a NEWFIRM Brγ image of 30 Doradus, our data reveal the morphologies of the warm molecular gas and ionized gas in 30 Doradus. The brightest H_2-emitting area, which extends from the northeast to the southwest of R136, is a photodissociation region viewed face-on, while many clumps and pillar features located at the outer shells of 30 Doradus are photodissociation regions viewed edge-on. Based on the morphologies of H_2 , Brγ , ^{12}CO , and $8\,\mu m$ emission, the H_2 to Brγ line ratio and Cloudy models, we find that the H_2 emission is formed inside the photodissociation regions of 30 Doradus, 2 – 3 pc to the ionization front of the H II region, in a relatively low-density environment $< 10^4$ cm^{-3}. Comparisons with Brγ , 8 μm, and CO emission indicate that H_2 emission is due to fluorescence, and provide no evidence for shock excited emission of this line.

1. INTRODUCTION

Starburst feedback is vital in galaxy evolution, as it is important in unbinding large molecular clouds (Krumholz et al. 2006; Fall et al. 2010; Murray et al. 2010), driving gravitational collapse inside molecular clouds and triggering sequential star formation (Elmegreen & Lada 1977; Oey et al. 2005; Zavagno et al. 2010), driving turbulent motions within the clouds (Matzner 2002), eroding molecular clouds by photo-evaporation (Whitworth 1979; Williams & McKee 1997; Matzner 2002), and determining emission line spectra of the photoionized regions (Binette et al. 1997; Dopita et al. 2005, 2006; Draine 2011; Yeh & Matzner 2012; Yeh et al. 2013; Verdolini et al. 2013). While the effects of massive star feedback have been extensively discussed in the literature, a critical piece of information is missing: how does energy and momentum feedback from massive stars affect the molecular clouds' physical properties? We focus on the spatial distribution of molecular and ionized hydrogen emission, signals which highlight ionization fronts and working surfaces in this region of active stellar feedback.

A prime site for the origin of H_2 emission is at the boundary of ionized gas, shocks, and molecular clouds, which is the working surface for many forms of stellar feedback into the dense gas. Because the excitation of H_2 molecules is sensitive to the density structure, radiation hardness, or mechanical energy input from shocks, H_2 ro-vibrational transitions are unique tracers to probe physical properties of the ISM under massive star feedback. The 30 Doradus nebula (30 Dor) in the LMC is a well-studied and one of the nearest (50 kpc) starburst regions, at which distance a very high spatial linear resolution ($1'' = 0.2$ pc) can be achieved. The

30 Dor nebula is dominated by the very young star cluster R136, which produces $10^{51.6}$ hydrogen-ionizing photons per second (Crowther & Dessart 1998), ionizing neutral material and driving it outward. Although the Dragonfish Nebula (Rahman et al. 2011) and NGC 3603 (Conti & Crowther 2004) are much closer (< 10 kpc) and produce hydrogen-ionizng luminosities of $10^{51.8}$ and $10^{51.5}$ s^{-1}, respectively, 30 Dor's convenient location out of the galactic plane allows a straightforward comparison to more distant starburst regions. Many observations of 30 Dor have been presented in the wavelengths from the X-ray to radio (Townsley et al. 2006; Chu & Kennicutt 1994; Poglitsch et al. 1995; Rubio et al. 1998; Indebetouw et al. 2009; Johansson et al. 1998; Indebetouw et al. 2013), however, a fully calibrated H_2 map of the entire 30 Dor has never been produced. Wide field of view images of multiple ISM components are critical for followup studies on dynamics of the region, and for the selection of sites for targeted observations, such as high-resolution spectroscopy and interferometric studies, which necessarily involves smaller fields of view.

Observations of H_2 in parts of 30 Dor have been done by Poglitsch et al. (1995) (P95) and Rubio et al. (1998) (R98). P95 reported that the H_2 1–0 S(1) morphology appeared fragmented ($\sim1''$, 0.2 pc clumps), and suggested that the emission originated from dense molecular clumps. The P95 data is observed in a $3'\times3'$ area in 30 Dor, which is a very small fraction of the region, while the R98 H_2 data were collected in a small area ($< 2'\times2'$) and not calibrated. These observations were limited in sensitivity and field of view by the instruments available at the time, and the photodissociation region (PDR) physical conditions derived from P95 and R98 do not fully represent that in the entire 30 Dor.

In this paper, we present the first fully calibrated H_2 1–0 S(1) image as well as a Brγ image of the full nebula, with a $1.0''$ angular resolution. We describe the observations and data reduction in § 2. In § 3, we show the H_2 and Brγ morphologies and determine line ratios, identify areas of interest for further analysis, and

E-mail: yeh@naoj.org
[1] Subaru Telescope, National Astronomical Observatory of Japan, 650 North A'ohoku Place, Hilo, HI 96720, USA
[2] Department of Astronomy & Astrophysics, University of Toronto, 50 St. George St., Toronto, ON M5S 3H4, Canada
[3] Department of Physics and Astronomy, University of Toledo, 2801 West Bancroft Street, Toledo, OH 43606, USA

investigate the spatial relations between H_2 and $Br\gamma$. In § 4, we present photoionization models using Cloudy, in order to constrain the range of physical parameters inside the 30 Dor PDRs by comparing the modeled and observed H_2 to $Br\gamma$ line ratio, and to explore the issue of bright line contamination we discovered during data reduction in the H_2 image. The origin of the H_2 1–0 S(1) emission is discussed in § 5. Finally, we summarize the paper in § 6. In the paper, all H_2 emission refers to the H_2 1–0 S(1) transition, unless indicated otherwise.

2. OBSERVATIONS AND DATA REDUCTION

We observed 30 Dor using the NOAO Extremely Wide-Field Infrared Imager (NEWFIRM; Probst et al. (2008)) on the CTIO 4-meter Blanco Telescope, over three half-nights on November 10, 11, and 12, 2010. NEWFIRM has a field of view of $28' \times 28'$, and its pixel scale is $0.4''$ per pixel. The H_2 1–0 S(1) ($2.12\,\mu m$) and $Br\gamma$ ($2.17\,\mu m$) emission line data were taken using the 2124 nm H_2 and 2168 nm $Br\gamma$ narrow band filters, respectively. See Table 1 for filter parameters. The broad-band continuum data were collected using the Ks filter. The total exposure time of the H_2 image was 210 minutes, and 14 minutes for the $Br\gamma$ image. The observations were dithered in a random pattern in a $30''$ box to fill the gaps between detector arrays. The photometric standard star S121-E was observed in both 2124 nm and 2168 nm filters to serve as the flux calibrator. Table 1 summarizes details of the observations. Because the angular size of 30 Dor in the sky is about the same as the size of NEWFIRM field of view, in order to obtain sky images free of nebular emissions, we nodded the telescope on and off[4] the target following the sky-target-target-sky sequence.

Data reduction was carried out using the NEWFIRM pipeline V1.3 (Swaters et al. 2009). Dark subtraction was first applied to the data, followed by a linearity correction and flat fielding. Sky background was determined by taking the median of four preceding and four subsequent off-source sky exposures which are free of extended emission, and the background level was scaled to match that in target images and then subtracted. An astrometric solution was obtained using the 2MASS catalogue, and all images were re-projected and stacked. The sky background was then redetermined and subtracted by masking objects (including stars and extended nebular emission) detected in the first pass, and new stacks of images were produced.

2.1. PSF Matching

We carried out a photometric analysis of field stars using the software package SExtractor (Bertin & Arnouts 1996). Stars with detection higher than 5σ in areas free of extended nebular emission are identified by SExtractor, and their photometric parameters, such as flux and FWHM, are recorded in catalogs. We first extracted the mode of the distribution of FWHM in each stacked image, namely $Br\gamma$, H_2, and Ks images, as the representative seeing in each image. It showed that $Br\gamma$ and Ks images have better seeing ($< 1.0''$) than the H_2 image. We then convolved the $Br\gamma$ and Ks images with

---

[4] The telescope was nodded off-target 1 degree north of R136.

---

gaussian kernels until the convolved FWHM matches that of the H_2 image. After the gaussian convolution, the seeing in H_2, $Br\gamma$, and Ks images is $1.0''$, and this is the resolution in every image presented in the paper unless indicated otherwise.

2.2. Flux Calibration

The standard star S121-E (Persson et al. 1998) was observed as a flux standard. The $Br\gamma$ and H_2 filters are centered closely at the Ks filter central wavelength, and we apply the magnitude-to-flux density conversion factors derived from the S121-E data, to flux calibrate the 30 Dor data. Data were taken under stable weather and nearly constant airmass, therefore the major uncertainties of measured fluxes come from bright emission line contamination in the Ks filter, which are discussed in § 2.3.1.

2.3. Continuum Subtraction

To produce emission line images, one must subtract continuum emission in the narrowband (NB) data. The ideal way to subtract continuum in a NB image is to use an off-line center NB filter with identical FWHM, and such NB image shows continuum without contamination of any emission lines. However, off-line NB filters were not available when the observations were carried out, we therefore carried out continuum subtraction using the broadband (BB) Ks data.

Mathematically, the observed fluxes in each filter ($2.12\,\mu m$, $2.16\,\mu m$, and Ks) can be expressed as

$$F_{2124} = F_{H_2} + F_{ct_{2124}} \ \ ,$$
$$F_{2168} = F_{Br\gamma} + F_{ct_{2168}} \ \ ,$$
$$F_{Ks} = F_{H_2} + F_{Br\gamma} + F_{uk} + F_{ct_{Ks}} \ \ ,$$

where F_{2124}, F_{2168}, and F_{Ks} are fluxes measured in the $2.12\,\mu m$, $2.16\,\mu m$, and Ks filters, respectively. The convention 'ct' labels the continuum emission fluxes measured in a filter, and 'uk' marks unknown emission line fluxes contained within the Ks filter.

Continuum subtraction in $Br\gamma$ and H_2 images then will produce:

$$F_{2168} - \alpha F_{Ks} = F_{Br\gamma} + F_{ct_{2168}} - \alpha(F_{H_2} + F_{Br\gamma} + F_{uk} + F_{ct_{Ks}}) \ \ ,$$

yielding

$$F_{Br\gamma} = \frac{F_{2168} - \alpha(F_{Ks} - F_{H2} - F_{uk})}{1 - \alpha} \ \ , \quad (1)$$

and

$$F_{2124} - \beta F_{Ks} = F_{H_2} + F_{ct_{2124}} - \beta(F_{H_2} + F_{Br\gamma} + F_{uk} + F_{ct_{Ks}}) \ \ ,$$

yielding

$$F_{H_2} = \left[\frac{F_{2124} - \beta(F_{Ks} - F_{Br\gamma})}{1 - \beta} \right] + \frac{\beta}{1 - \beta} F_{uk} \quad (2)$$

where $\alpha F_{Ks} = F_{ct_{2168}}$ and $\beta F_{Ks} = F_{ct_{2124}}$. The equations are applicable at every pixel in the image. The values of α and β in principle should be close to the FWHM ratio of the $Br\gamma$ to Ks filter and H_2 to Ks filter, respectively.

Table 1
30 Doradus Observation Summary

Line	Vacuum Wavelength	Filter FWHM (nm)	Filter name	Observed Dates[a]	Total Integration Time (minutes)
Ks continuum	$\cdots$	320.0	Ks	Nov 10, 12	22
H_2 1–0 S(1)	2.121 μm	24.0	2124 nm	Nov 10, 11, 12	210
Brγ	2.166 μm	24.4	2168 nm	Nov 11	14

[a] Data were taken in year 2010.

We determine α and β empirically by evaluating the stellar flux ratio of 2.16 μm to Ks, and 2.12 μm to Ks. We employed SExtractor to extract stellar fluxes in the 2.12 μm, 2.16 μm, and Ks images. The scaling factor α and β are 0.07 and 0.08, respectively, which is in good agreement with the filter FWHM ratios. The above equations are correct when the CCD response is linear in all three filters. However, stars with counts $> 10,000$ Analog/Digital Units are saturated, i.e. the CCD response becomes nonlinear, and they cannot be completely subtracted. Therefore we exclude these stars in the analysis.

We found that the BB Ks data contain Brγ , H_2 , and possibly other emission lines, as well as the continuum emission, which introduce contamination. We evaluate and discuss the bright line contamination issue in § 2.3.1.

2.3.1. *Bright Emission Line Contamination*

No direct information is available to us on the possible emission lines that, other than Brγ and H_2 , might contribute to the Ks filter emission. However, He I is a likely candidate since it is observed in other star forming regions. For example, helium emission lines are reported in M16 in the 2 μm regime (Levenson et al. 2000, hereafter L00), in addition to Brγ and H_2 lines. Amongst the detected emission lines, Brγ is the brightest in M16, and a bright He I line at 2.06 μm is 70% of the total flux of Brγ . If the He I -to- Brγ ratio is the same in 30 Dor as in M16, the contamination from He I in the Ks filter will be noticeable.

Brγ emission line in 30 Dor is likely the brightest amongst the emission lines in the Ks filter. If the He I line has the same relative strength in 30 Dor as in M16 (70%), Equation 1 shows that it is equivalent to about 5% of the continuum-subtracted Brγ emission, assuming it is distributed in the same way. Therefore continuum subtraction in the Brγ image may not be severely affected by bright emission line contamination, and Equation 1 can be approximated as

$$F_{Br\gamma} \simeq \frac{F_{2168} - \alpha F_{Ks}}{1 - \alpha} \quad . \tag{3}$$

In the case of H_2 continuum subtraction, however, bright emission line contamination becomes significant. Following Equation 2, the first-pass continuum subtracted H_2 shows that if no correction was made, then there would be a noticeable over-subtracted area. Indeed, without correction, we noticed a region of negative emission representing the Brγ emission in the vicinity of the nebula. With careful visual inspection, we found that the negative components well resemble the morphology of the highest surface brightness Brγ emission. We then inspected the first-pass continuum subtracted H_2 and Brγ images on the pixel-to-pixel basis, comparing the pixel values of the negative component in the H_2 image

to the Brγ image. There is a tight correlation between the negative H_2 pixels and brightest Brγ pixels, confirming that the majority of over-subtraction comes from line emission which correlates strongly with Brγ emission.

Let

$$F'_{H_2} \equiv \frac{F_{2124} - \beta(F_{Ks} - F_{Br\gamma})}{1 - \beta} \quad \text{and}$$

$$\xi F_{Br\gamma} \equiv F_{uk} \quad ,$$

Equation 2 can be rearranged as

$$F'_{H_2} = F_{H_2} - \frac{\beta}{1 - \beta} \xi F_{Br\gamma} \quad . \tag{4}$$

The slope $\frac{\beta}{1-\beta}\xi$ in Equation 4 is -0.10, evaluated from fitting the residual data. Therefore we correct continuum subtraction of the H_2 image by

$$F'_{H_2} = F_{H_2} - (-0.10)F_{Br\gamma}$$

We inspected the pixel values of the corrected H_2 image F'_{H_2}, and the majority of the negative pixels after the correction have values around 0. In fact the factor 0.10 is higher than the expected value $\beta/(1-\beta) = 0.087$, which indicates that we have not only corrected for the contamination introduced by the Brγ emission, but also the contamination from other unknown bright emission lines. The bright-line contamination is thus $(0.10-0.087)/0.087 = 0.15$, or 15% of the Br$\gamma$ emission flux, which corresponds to 1.3% of the continuum flux.

We found that, after correcting the H_2 image for the contamination, some negative pixels still persist in the areas very close to R136. Those pixels can only be corrected by $\frac{\beta}{1-\beta}\xi = 0.14$, instead of 0.10 in Equation 4. However this leads to over-correction in the image, i.e. bright Brγ features become prominent in the H_2 image, which indicates that the contaminating emission is stronger relative to Brγ near the cluster than further away. The corresponding total brightness of this contamination is 61% of the Brγ flux, assuming that the emission line flux is distributed in the Ks band in the same way as Brγ , which leads to additional 4% of the continuum flux, which is also the uncertainty in the contamination-corrected H_2 image. We suspect that the He I line at 2.06 μm is the major source of continuum contamination other than Brγ , and its contamination becomes more significant in the central region of 30 Dor. Several He I lines are detected in the M16 H II region, in addition to Brγ and H_2 1–0 S(1) (L00). As noted earlier, the brightest He emission line detected in M16 in the K band is He I at 2.06 μm, and its flux of the He I line is 70% of the total flux of Brγ . The 61% of the Brγ flux contamination we have empirically estimated for the region near R136 is as significant as that in the M16 case. Note that variations in the continuum slope,

such as those induced by variations in extinction, will also not be consistent with constant values of our α and β parameters.

We do not have any He line data in 30 Doradus to constrain the degree of contamination, therefore we turn to Cloudy simulations to explore this issue, which is discussed in § 4. In this paper, the H_2 image is empirically corrected for contamination following Equation 4.

3. RESULTS

3.1. H_2 and $Br\gamma$ Morphologies

Fully calibrated H_2 and $Br\gamma$ images of 30 Dor are presented in a 3-color composite image in Figure 1. Red is H_2, blue is $Br\gamma$, and green is the Ks band continuum. Both $Br\gamma$ and Ks are stretched logarithmically to emphasize areas of highest surface brightness, while H_2 is displayed in the linear scale because the line brightness dynamic range is much smaller. The star cluster R136 is marked by a black circle. Note that the pulsar wind nebula N157B, which is located at the same distance and $7'$ to the southwest of 30 Dor, is also present in the image. In this paper we focus only on the analysis of 30 Dor and will ignore N157B.

The $Br\gamma$ emission reveals the spatial distribution of ionized gas in 30 Dor. Areas with highest surface brightness appear to trace an arch structure extending from northeast to southwest of the R136 cluster, consistent with the ionized gas morphology reported in the literature (Chu & Kennicutt 1994; Poglitsch et al. 1995; Pellegrini et al. 2010). To the north and west of R136, $Br\gamma$ appears quite filamentary and its surface brightness becomes lower. To the southeast of 30 Dor, the $Br\gamma$ morphology reveals multiple shell structures, enveloping pillars and clumpy features. The total flux in an area $3.1' \times 3.7'$ is measured as 1.02×10^{-10} erg s^{-1} cm^{-2}. Although this is higher than the total $Br\gamma$ flux reported in P95 (4×10^{-11} erg s^{-1} cm^{-2}) measured in the same area, our $Br\gamma$ image detects fainter structure than that in the P95 image.

The most prominent H_2 emission is seen to the northeast of R136, in conjunction with the bright $Br\gamma$ arch and coincident with lower surface brightness $Br\gamma$ emission. This prominent H_2 emitting area, which is also known as 30Dor-10 (e.g. Johansson et al. 1998; Indebetouw et al. 2009, 2013), also marked as Area A in Fig. 1, spans at least $3'$ by $3'$ in the plane of the sky, which corresponds to 36×36 pc at a distance of 50 kpc. The H_2 emission in 30Dor-10 seems somewhat disordered and extended, with clumps close to R136 and filaments extending away from R136. The total H_2 flux measured in the area is 5.16×10^{-12} erg s^{-1} cm^{-2} after masking bright saturated stars. The H_2 emission to the west of R136 appears much clumpier and mixed with high surface brightness $Br\gamma$ emission. To the north and northeast of R136 (Area B), H_2 appears in the form of filaments which seem to form a chimney pointing away from R136, and their morphology is poorly correlated with the $Br\gamma$ filaments in the same area. Prominent pillar features are seen in the southeast of R136, pointing towards the ionizing source R136 and are encompassed by the $Br\gamma$ emission, such as that in Area C. These $Br\gamma$ envelopes have sharp outer boundaries, with radii of curvature significantly greater than those of the H_2 pillars they envelop. This is sugges-
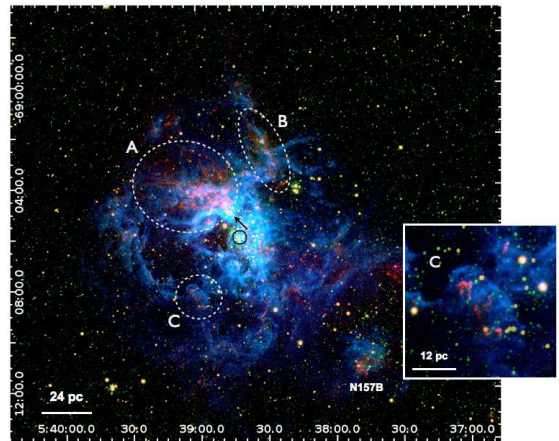

Figure 1. Three-color composite image of 30 Doradus. North is up and East is to the left. Red: H_2, displayed in linear scale; green: Ks continuum in logarithm stretch; blue: $Br\gamma$ in logarithm stretch. R136 is marked by a black circle. The seeing is $1.0''$. H_2-emitting areas of interest are marked by white dashed ellipses, including (A) the bright H_2 band to the northeast of R136, (B) filaments pointing north-ward of R136, and (C) pillars to the southeast of R136. A zoomed-in figure of Area C is shown on the right. A bright H_2 finger in Area A is indicated by a black arrow.

tive of a photo-evaporative flow bounded by the pressure of hot gas. No H_2 emission was detected to the northwest of R136. Overall, the $Br\gamma$ and H_2 emission appear to form walls of the cavities or holes seen in 30 Dor. The observed H_2 emission is located well within the nebula (defined by optical broadband data). We will discuss Area A, B, and C in detail in § 3.2.

3.2. Areas of Interest

We identified areas of interest for further analysis by comparing the H_2, $Br\gamma$, and ^{12}CO morphologies as shown in Figure 2 and Figure 1. The H_2 and $Br\gamma$ data were superimposed with the ^{12}CO 1–0 data of 30 Dor (Wong et al. 2011)[5]. The $Br\gamma$ image in Figure 2 is displayed in grayscale to guide the reader's eyes on the ionized gas morphology, while the H_2 contours are convolved to a $4.5''$ resolution. We found that bright H_2-emitting areas spatially correlate very well with the bulk of CO emission (Figure 2). Based on the morphological correlation between H_2 and CO emission, and H_2 and $Br\gamma$ emission, three areas are identified as areas of interest: (1) Area A: the northeastern band of H_2 emission with highest H_2 surface brightness, and it spatially coincides with the brightest CO emission in 30 Dor. This area is also known as 30Dor-10 as noted earlier; (2) Area B: the filament pointing north and away from R136, which is relatively bright and spatially correlated well with the peak of CO emission in the same area; and (3) Area C: pillars to the southeast of R136 at the outer shell of 30 Dor, which have clearly defined morphology in the H_2 emission and are surrounded by $Br\gamma$-emitting envelopes; no CO emission is detected in this area (by the ATNF

[5] We chose the Wong et al. (2011) CO data for comparison instead of the Indebetouw et al. (2013) ALMA data, because we are interested in the CO distribution in the entire 30 Dor. The ALMA image field of view is too small, and the interferometric data is not sensitive to extended structures. Nevertheless, the ALMA data will be useful for detailed studies of smaller objects of interest in the region.

Mopra Telescope, Wong et al. (2011)). A zoomed-in figure of Area C is shown in Figure 1.

H_2 was detected in an earlier observation (P95) in the western part of Area A, in a much smaller $2' \times 2'$ area. The H_2 morphology observed by P95 was reported very clumpy, which is consistent with the H_2 morphology shown here (Figure 1). The peak H_2 surface brightness in the P95 result is $5.41 \times 10^{-15}\,\mathrm{erg\,s^{-1}\,cm^{-2}\,arcsec^{-2}}$. However, this peak intensity arises from a bright star in the field thus may not be reliable. In our wide-field observations, more H_2 emission is seen towards the eastern part of Area A. After excluding bright saturated stars, the maximum H_2 surface brightness is measured $2.15 \times 10^{-15}\,\mathrm{erg\,s^{-1}\,cm^{-2}\,arcsec^{-2}}$. H_2 in Area A also coincides with the bulk of CO emission in 30 Dor (Wong et al. 2011) (Figure 2). No H_2 emission is seen completely uncorrelated with either the Brγ or ^{12}CO 2–1 emission. With only one ro-vibrational transition of H_2 emission, and without making further assumptions, we estimated mass contained in the upper state of the observed H_2 transition in Area A to be 0.01 $M_\odot$, estimated with the Einstein A coefficient $A_{S(1)} = 2.09 \times 10^{-7}$ $\mathrm{s^{-1}}$ (Turner et al. 1977; Wolniewicz et al. 1998). [6] This mass is orders of magnitude lower than the molecular mass estimated from CO emissions of 8.5×10^4 $M_\odot$ (Pineda et al. 2012; Johansson et al. 1998), which implies that the observed H_2 emission requires the existence of only a negligible fraction of the total molecular mass.

Area B also shows high H_2 intensity, and the maximum H_2 surface brightness in this area is $6.44 \times 10^{-16}\,\mathrm{erg\,s^{-1}\,cm^{-2}\,arcsec^{-2}}$. This region was outside the field of view of the P95 observations. Area B lines up well with its CO counterpart (Figure 2), similar to Area A.

Area C was outside the field of view of the P95 observations as well. The peak surface brightness is measured $1.76 \times 10^{-15}\,\mathrm{erg\,s^{-1}\,cm^{-2}\,arcsec^{-2}}$, comparable to that measured in other areas. Although Area C does not appear to have any CO counterpart, its H_2 emission indicates the presence of molecular clouds in that area. The morphology of the pillars is very similar to the ones observed in smaller H II regions, such as M16 (Hester et al. 1996, L00). We highlight few interesting morphological features in Area C, which will lead to followup detailed studies of the region: (1) the H_2 emission is enclosed within the Brγ emission which extends toward R136, (2) the H_2 emission appears at the leading edge of regions where other molecular cloud tracers are present, such as the 8 μm emission, and (3) the Brγ emission is bounded by a sharp outer boundary whose radius of curvature is significantly larger than that of the H_2, which implies possible pressure confinement by hot gas. A crude estimate of the projected distance between the Brγ envelopes and the pillars is ~ 3 pc. Area C's neighbor clumps also show similar separation between Brγ and H_2. We will return to discuss this point in § 5.1.

3.3. The Spatial Relationships Between Ionized and Molecular Gas in 30 Doradus

[6] Note that this mass estimate yields a lower limit of molecular mass, because it does not include the mass associated with all other levels.
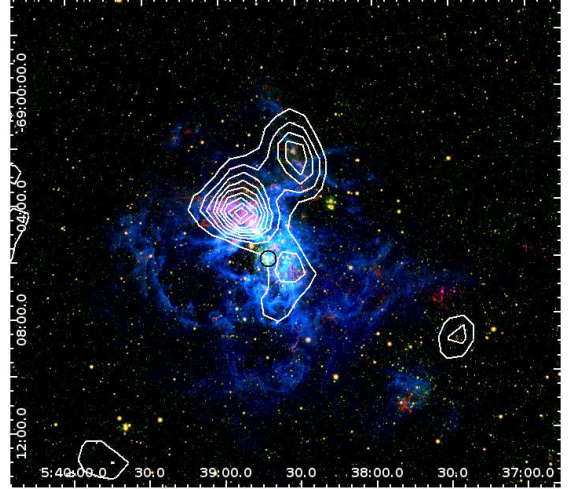

Figure 2. CO 1–0 contours (white contours, Wong et al. 2011) superimposed on the 3-color composite image as shown in Figure 1. The CO contours start at 10% of the peak intensity (12.4 K km s^{-1}) and increase in 10% steps. The CO data angular resolution is 60″. R136 is marked by a black circle.

The overall morphology of the observed H_2 emission is well correlated with the Brγ distribution within 30 Dor – when Brγ emission is present, H_2 emission is either seen very nearby the Brγ emission, such as the outer shells and pillar features, or appears to be a counterpart of the Brγ emission, such as Area A and the region just west of R136.

Bright H_2-emission is seen to be spatially coincident with the Brγ emission in Area A (Figure 1), except for an excess of Brγ emission around the limb of the "finger" seen in H_2. This suggests that we are viewing the H II region roughly face-on, except around the limb. Furthermore, the CO-emitting gas in the core of the finger is likely to be marginally optically thick at $2.2\,\mu$m, judging from the ALMA observations of ^{13}CO presented by Indebetouw et al. (2013). They estimate ^{13}CO column densities $> 5 \times 10^{15}\,\mathrm{cm^{-2}}$ along this finger (and clumps an order of magnitude higher column; their Fig. 10), and adopt $N_{H_2} = 5 \times 10^6 N_{^{13}CO}$; along with a dust opacity of roughly $1.3 \times 10^{-20}\,\mathrm{cm^2}$ per H atom at $2.17\,\mu$m (Weingartner & Draine 2001), we estimate the characteristic optical depth of the finger to be ~ 0.65. It is therefore quite likely that most of the observed emission is emitted on the Earthward side of the molecular finger. The absence of obvious shadows associated with high-column clumps of ^{13}CO corroborates this interpretation.

On a similar basis, we infer that emission seen just west of R136 is likely to originate from behind the cluster (as seen from Earth), on the basis that the Wong et al. (2011) CO contours extend into this region. This geometry is further supported by recent optical emission line studies by Pellegrini et al. (2011)(P11). With optical emission line ratios together with modeled ionization parameters, P11 suggests that Area A and the region just west of 30 Dor are located 60 pc behind R136.

Area B may share the same geometry as the regions we discussed above – this filament of molecular gas should be behind the Brγ emission and R136. Although the Brγ morphology is filamentary with rather poor correlation with the H_2 emission, Brγ is seen to partially

coincide with the H_2 and CO emission in the area, instead of being on the edge of molecular clouds. This suggests that the $Br\gamma$ emission is not shielded by molecular clouds, and we are viewing this region face-on. Lacking high-resolution CO data, however, we cannot draw this conclusion with certainty.

Area C is likely oriented differently relative to 30 Dor than are Areas A and B. The bright $Br\gamma$ emission in this region shows relatively poor spatial correlation with the H_2 emission. $Br\gamma$ is seen closer to R136 in the projected plane of sky, and it envelops the H_2 emission, which has a relatively small projected area. Although $Br\gamma$ extends outward from the H_2 emission (and toward 30 Dor) to a similar degree here as in Areas A and B, the much smaller H_2-emitting regions give it more of the appearance of an evaporation flow.

In all three regions there are locations where $Br\gamma$ emission extends away from a boundary of the H_2 emission, generally in the direction toward 30 Dor, before terminating at an enclosing boundary about two to three parsecs away. To be specific, in Figure 1 we measure projected standoff distances of 2.5 pc perpendicular to the finger in Area A (to the southeast); of 2.2 pc (toward 30 Dor) from the small H_2 blob at the southern end of Area A; of about 1.9 pc (toward 30 Dor) from parts of the H_2 ridge in Area B; and of 1.9 pc (toward 30 Dor) and 2.2 pc (perpendicularly to the northeast) from the H_2 pillars in Area C. All of these characteristics – the tendency of $Br\gamma$ emission to enclose H_2, its tendency to extend a few parsecs toward 30 Dor, and its tendency to meet a sharp boundary, are expected to reflect the physical origin of these two types of emission, as well as the relative importance of effects such as photo-evaporation and confinement by stellar wind pressure.

3.4. H_2 to $Br\gamma$ Line Ratio

The morphological relations between H_2, $Br\gamma$, and CO emission are indicative that the observed H_2 emission traces the PDRs in 30 Dor. With data of only one H_2 emission line, we do not have sufficient information to firmly constrain the physical quantities in the PDRs. Nevertheless, the line ratio of H_2 to $Br\gamma$ is a useful guide to delineate the spatial distribution and structure of molecular gas relative to ionized gas in the PDRs, especially when a PDR is viewed face-on. Combining with numerical modeling efforts, the observed H_2 to $Br\gamma$ line ratio offers a hint of the physical properties of molecular and ionized gas in 30 Dor.

A line ratio map H_2 to $Br\gamma$ is shown in Figure 3. Pixels in the $Br\gamma$ image were clipped at a 3σ level, and pixels with S/N higher than 50σ[7] detection in the H_2 image were masked in order to exclude bright saturated stars. A line ratio map then was convolved to a $4.5''$ resolution with a gaussian kernel.

Overall, areas with higher H_2 / $Br\gamma$ ratios in 30 Dor are clumpy with ratios of 0.2 to 0.5. Most areas show lower H_2 / $Br\gamma$ ratio ~ 0.1, which agrees with the same line ratio observed in M16 (L00, derived from the total fluxes). Higher H_2 / $Br\gamma$ ratios are seen in Area A, Area B, filaments north of Area B, and some isolated pillar features (including Area C) at the outer shells of 30 Dor.

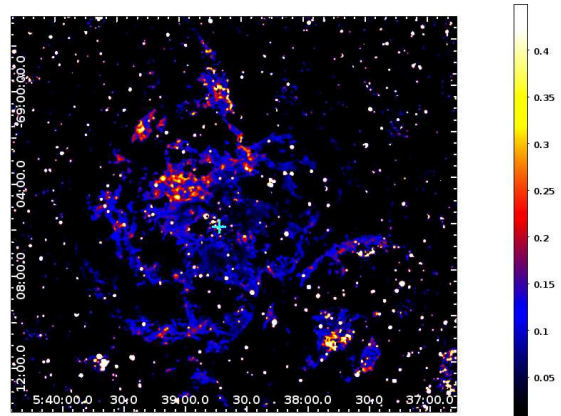[7] An empirical value to mask saturated bright stars.

Figure 3. H_2 to $Br\gamma$ line ratio map of 30 Dor, convolved by Gaussian kernels to a $4.5''$ resolution. The colorbar marks the H_2 to $Br\gamma$ ratio; R136 is marked by a cyan cross.

In Area A, the H_2 to $Br\gamma$ ratio across the area appears clumpy, with some localized high line ratio areas and 'voids'. The maximum ratio is 0.5, and the overall ratio is > 0.2. The clumpy H_2 distribution and H_2 to $Br\gamma$ line ratios seen in Area A indicate that FUV radiation could penetrate deeper into the molecular clouds. The maximum line ratio at Area B is 0.45, and the overall radio is ~ 0.3. The line ratio morphology suggests that $Br\gamma$ across this area is fairly filamentary. Area C displayed a high H_2 to $Br\gamma$ line ratio of 0.3, which coincides with the bright H_2-emitting area at the tip of the pillars.

We note that the two ISM components traced by $Br\gamma$ and H_2 arise in adjacent but noticeably separate areas, and the local, apparent line ratios are subject to significant projection effects. The projection effect is most severe in regions where the ionized gas envelops a molecular pillar viewed edge-on, such as in Area C.

4. PHOTOIONIZATION MODELS

4.1. Motivations

Our main motivation to carry out numerical simulations is to explore a wide range of physical conditions in H II regions and PDRs, and obtain emission line intensities as a function of physical conditions. The observed $Br\gamma$ and one single H_2 emission provide very limited information, but with numerical simulations, we are still able to learn something useful about the physical conditions in 30 Dor. Another motivation is to explore the issue of bright emission line contamination in the data. A series of H_2 emission lines, hydrogen recombination lines, and He recombination lines are present in the $2\,\mu m$ regime. We found evidence of additional emission line contamination (other than $Br\gamma$) in the Ks continuum, affecting continuum subtraction in the H_2 image (see § 2.3.1). We have empirically corrected for the contamination, and the estimated contamination level is in good agreement with similar type of observations in other H II regions. Numerical simulations are helpful to investigate feasible origins of contamination and consequences.

4.2. Model Parameters

We generated models of simple H II regions to study emission line intensities and physical conditions of molecular clouds in 30 Dor. First we used Starburst99
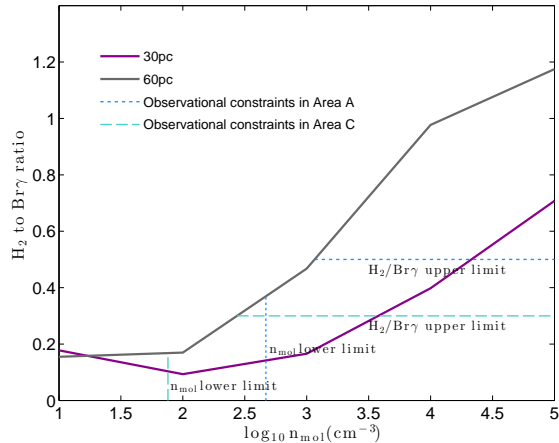
Figure 4. H_2 1–0 S(1) to Brγ line ratios as a function of molecular gas density (n_{mol}) and distance to the ionizing source. The purple line shows H_2 to Brγ line ratio computed at a distance of 30 pc, and the line ratio computed at 60 pc is shown in the gray line. Observational constrains on H_2 to Brγ ratios and n_{mol} in Area A and C are marked by blue dotted and cyan dashed lines, respectively.

(Leitherer et al. 1999) to generate ionizing continuum spectra of a massive coeval star cluster at 2 Myr age, because the age of R136 is $\lesssim$ 2 Myr (de Koter et al. 1998; Massey & Hunter 1998). The star cluster is assumed to be massive enough to fully sample the initial mass function, which has exponents -1.3 and -2.3 between stellar mass boundaries of 0.1, 0.5, and 120 M$_\odot$. We employed the Geneva high mass-loss evolutionary tracks with 0.4 solar metallicity. The Geneva high mass-loss tracks are optimized for modeling atmospheres of high mass stars and are recommended by Maeder & Meynet (1994). We adopt Pauldrach/Hillier atmospheres and the LMC UV line library. The atmospheres include non-LTE and line-blanketing effects (Smith et al. 2002) for O stars (Pauldrach et al. 2001) and Wolf-Rayet stars (Hillier & Miller 1998).

Starburst99 output continuum spectra are fed into Cloudy 08.00[8] as the ionizing continuum of each simulated H II region. Pellegrini et al. (2010, 2011) suggested that the inner 15 pc of 30 Dor lacks ionized gas and thus molecular clouds. The ionization front near Area A identified in Pellegrini et al. (2010) is located at a projected distance of 30 pc, and materials behind the star cluster R136 are at a characteristic distance of 60 pc. We therefore set the inner radius of the simulated H II regions at 30 pc and 60 pc with respect to the ionizing source[9]. A wide density grid $\log(n_H)=1$ to 5 is incorporated in the calculations. We adopt the dust grain size distributions of the LMC (Pellegrini et al. 2011; Weingartner & Draine 2001), and Cloudy's default ISM abundances at 0.4 solar metallicity. Each calculation stops when the cloud temperature drops to 30 K, well inside a PDR. Integrated line luminosities, Brγ at 2.17 μm, He I at 2.06 μm, H_2 1–0 S(1) at 2.12 μm, H_2 1–0 S(0) at 2.22 μm, and H_2 2–1 S(1) at 2.25 μm, are calculated and recorded.

---

[8] Calculations were performed with version 08.00 of Cloudy, last described by Ferland et al. (1998).

[9] Regions modeled at a projected distance < 10 pc would require ionizing sources other than R136 (Pellegrini et al. 2011).

5. MODEL RESULTS AND DISCUSSION

With the model parameters indicated in § 4.2, we first modeled H II regions under perfect force balance between thermal pressure of the cloud and incident radiation and wind pressure. At the distance 30 pc and 60 pc away from the ionizing source, ionized gas density in the force-balanced H II regions appears constant, however, in the PDR region the cloud pressure can become unrealistically high when the ionized gas density is high. This is because our simple models do not include turbulence and magnetic field pressure terms, which are important in supporting molecular clouds. The modeled regions thus form artificially high thermal pressure beyond the ionization front (IF) in order to meet the force balance criterium. To resolve this problem, we turned to the constant density model. The Brγ emission intensities calculated in both force balance and constant density models are consistent to within 1%, therefore it is reassuring that the constant density models adequately represent the emission line spectra in the ionized gas, which is important in affecting the FUV spectra entered into PDR. We generated tables of emission line intensities as a function of the density grid and interpolated the observed line ratios using such tables, to obtain plausible range of physical conditions in 30 Dor.

5.1. *Molecular Gas Density*

We also modeled simple H II regions with parameters described in § 4 and computed the Brγ and H_2 1–0 S(1) emission intensities as a function of gas density $\log_{10} n_H$ = 1 to 5 (Figure 4). The computed H_2 to Brγ line ratios at 30 pc and 60 pc are shown in purple and gray lines, and the dotted and dashed lines mark observational constraints of molecular gas densities and H_2 / Brγ ratios in Area A and C. The lower limit of molecular gas densities is set by the ionized gas densities evaluated from the [SII] emission line doublet in Pellegrini et al. (2010) near the IFs at Area A and C. The ionized gas densities at those locations are found to be $10^{2.7}$ cm^{-3} and $10^{1.9}$ cm^{-3}, respectively. The upper limit of H_2 to Brγ line ratio in each area is set by our observations.

The H_2 to Brγ line ratio in most parts of Area A is < 0.5, implying that the molecular gas density is < 10^4 cm^{-3} at 30 pc and < 10^3 cm^{-3} at 60 pc. The maximum H_2 to Brγ ratio in Area A is $\sim$0.5, and the corresponding molecular gas density would be $\sim$$10^{4.3}$ and $10^{3.1}$ cm^{-3} at a distance 30 pc and 60pc, respectively. The simple comparison of observed and modeled line ratios suggests that H_2 in Area A is formed in relatively low density areas in the PDR of 30 Dor, close to the surface of the molecular cloud in conjunction to the IF, where ionized gas density is $\sim 10^{2.7}$ cm^{-3}. This is consistent with our findings in §3 that the observed H_2 emission arises from the PDR near IFs.

In the Area C pillars, the maximum H_2 to Brγ line ratio measured is 0.3, where H_2 emission intensity is also highest. The projected distance of Area C is greater than 30 pc, we therefore refer to the 60 pc model. At the upper limit of H_2 to Brγ ratio of 0.3, the molecular gas density would be $\sim$$10^{2.4}$ cm^{-3}. The Area C H_2 emission is seen with a projected separation of 3 pc from its Brγ envelope. With the ionized gas density $10^{1.9}$ cm^{-3}, a depth of 3 pc would corresponds to $A_V < 0.5$. One expects molec-

ular hydrogen to form inside a molecular cloud at depths $A_V \sim 0.13$ (van Dishoeck & Black 1988), which further supports the notion that the observed H_2 emission in Area C is formed inside the PDR but at a rather shallow depth. This conclusion holds just as well for the other locations where we have identified $Br\gamma$ extending 2-3 pc from an edge in the H_2 emission. As noted in §3.4, the apparent $H_2/Br\gamma$ line ratio determined on small scales is subject to projection effects because of this physical offset.

We can compare the observed H_2 emission fluxes with PDR models such as Sternberg & Dalgarno (1989)(SD89) and Black & van Dishoeck (1987)(BvD87), and constrain molecular gas densities in Area A, B, and C. The far UV radiation field χ in 30 Dor is $\sim 500\chi_0$ (Pineda et al. 2009; Anderson et al. 2014, where χ_0 (Draine 1978) relates to the Habing (1968) field by a factor of 1.71), while SD89 and BvD87 predicted that the H_2 1–0 S(1) intensity is $\lesssim 2\%$ of the total H_2 intensity at such radiation hardness. Adopting the average H_2 emission intensities at Area A, B, and C as 2% of the total H_2 intensity, the corresponding molecular gas densities in those areas are $< 10^4$ cm^{-3}, in coarse agreement with our Cloudy calculations. To firmly constrain molecular cloud densities in the 30 Dor PDR, we will need multiple ro-vibrational transitions of H_2 emission in followup studies. With one H_2 transition and $Br\gamma$, nevertheless, our analysis suggests that molecular clouds associated with the observed H_2 emission have densities $< 10^4$ cm^{-3}.

5.2. *Fluorescence or Shock Excitation? Origin of the H_2 1–0 S(1) Line Emission*

NIR molecular hydrogen emission lines in HII regions can form either via (1) pure fluorescence excitation or (2) shock heating, and the best way to distinguish fluorescence from shock excitation is to analyze multiple transitions of ro-vibrational molecular hydrogen emission lines. Although such spectroscopic data do not yet exist, the H_2 morphology, compared with CO morphology and H_2-to-$Br\gamma$ ratios, suggests no evidence of shock excitation.

As reported in § 3.1 and § 3.2, the H_2 morphology generally correlates well with that of CO. H_2 is likely to correlate poorly with CO emission in the case of shock excitation, which is often seen in star forming regions with active protostellar outflows. A good example is the Orion A giant molecular cloud (Davis et al. 2009).

The H_2-to-$Br\gamma$ line ratio is another diagnostic to distinguish fluorescence from shock excitation. In shock-dominated regions, the line ratio is often found greater than unity (Puxley et al. 2000; Medling et al. 2015); while in massive star-forming regions, the H_2-to-$Br\gamma$ ratio is < 0.6 (Joseph et al. 1984; Moorwood & Oliva 1988; Rodríguez-Ardila et al. 2004, 2005; Riffel et al. 2010). The reason behind the distinctive line ratios is fairly simple. Shocks cannot excite $Br\gamma$ emission, therefore in shock-dominated regions the H_2-to-$Br\gamma$ ratio will be high, regardless of viewing angle. On the other hand, UV radiation from massive stars excites $Br\gamma$ emission as well as H_2. $Br\gamma$ is often very bright, and when viewed face-on, one naturally finds relatively low H_2-to-$Br\gamma$ ratios. In 30 Dor, the line ratio is no greater than 0.5 (see § 3.4), which favors fluorescence as the dominant H_2

excitation mechanism. We note that in regions viewed edge-on where $Br\gamma$ is seen spatially offset from H_2, such as the pillars in Area C, the H_2-to-$Br\gamma$ ratio will be very low. Nevertheless, the presence of both $Br\gamma$ and H_2 excludes shock excitation, regardless of viewing angle.

5.2.1. *H_2 and 8 μm Emission Correlation*

The 8 μm emission adds additional information for diagnosing the origin of H_2 emission in 30 Dor. Emission at 8 μm is largely dominated by Polycyclic Aromatic Hydrocarbon (PAH) emission, which is excited by far-UV radiation in PDRs. Shocks, on the other hand, will destroy the PAH molecules and suppress the emission (Flower & Pineau des Forêts 2003; Micelotta et al. 2010). Therefore spatial and morphological correlations between the H_2 and 8 μm emission provide hints of the excitation mechanism of the observed H_2 emission. Good morphological correlations between the two distributions would suggest that H_2 emission is predominantly fluorescence excited, just like the 8 μm emission; poor morphological correlations would otherwise imply that the FUV radiation is not a major excitation source of the observed H_2 emission. The only excessive H2 emission related to shock activities is found near protostars at 4.5 μm, e.g. Cyganowski et al. (2008) and Lee et al. (2013).

We convolved the H_2 image and Spitzer IRAC 8 μm image to the same spatial resolution of 2.0″, and the superimposed image is shown in Figure 5. The H_2 emission is displayed in red, while the 8 μm emission is in green. The overall morphologies of H_2 and 8 μm emission correlate very well in the entire 30 Dor nebula, as well as in all three areas of interest A, B, and C. In Figure 6, we plotted the surface brightness of H_2 and 8 μm emission in Area A. The H_2 and 8 μm emission intensities also show a rather tight correlation. The good morphological and intensity correlations between H_2 and 8 μm emission strongly implies that the observed H_2 emission is predominantly excited by the FUV radiation in the PDR.

In several places within the nebula, especially Area C, H_2 and 8 μm emission highlight pillar structures. These are enclosed by thicker layers of ionized gas traced by $Br\gamma$ (noted in §3), which in turn have sharp boundaries that presumably arise from the pressure of the x-ray emitting hot gas. An example is shown in a zoom-in figure in Figure 1. In other locations, such as the finger in Area A, the 8 μm emission shares an inner edge with the $Br\gamma$ emission, as though the grains responsible for this emission permeate the photoionized gas. We intend to further pursue the physical interpretation of these correlations in a future paper.

5.3. *Bright Emission Line Contamination*

We use our models to further explore the bright emission line contamination issue in our H_2 image. $Br\gamma$ at 2.17 μm and H_2 1–0 S(1) at 2.12 μm are present in the modeled continuum spectra and are very close to the center of the Ks band filter, as expected. In addition, there are He I 2 ^1P–2 ^1S emission line at 2.06 μm, H_2 1–0 S(2) at 2.03 μm, H_2 1–0 S(0) at 2.22 μm, and H_2 2–1 S(1) at 2.25 μm. Table 2 summarizes the emission lines in the Ks band.
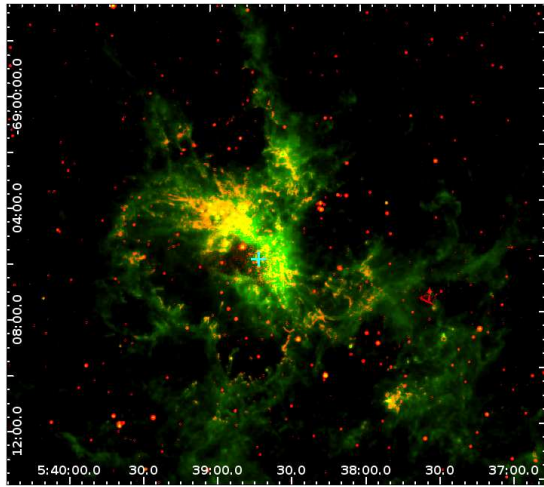
Figure 5. Spatial and morphological correlations between H_2 and $8\,\mu m$ emission in 30 Doradus. H_2 emission is shown in red, and the image is convolved to a $2.0''$ resolution to match that in the $8\,\mu m$ image. The $8\,\mu m$ emission is shown in green. R136 is marked by a cyan cross.
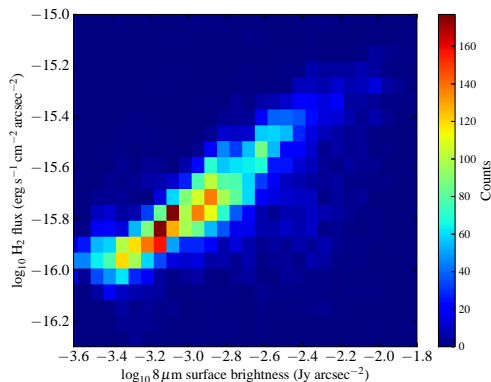

Figure 6. Surface brightness of H_2 and $8\,\mu m$ in Area A of 30 Doradus. The color bar indicates the number of pixels in each surface brightness bin of H_2 and $8\,\mu m$ data. The H_2 and $8\,\mu m$ intensities show an excellent correlation in this area, implying that the H_2 emission originated inside the PDRs.

The H_2 1–0 S(0), H_2 1–0 S(2), and H_2 2–1 S(1) lines are negligible, for they contribute $< 10\%$ of the Brγ flux in the Ks band. The He I line is the most plausible source of continuum contamination in our data. The calculated line ratios He I to Brγ at densities $< 10^4$ cm^{-3} are 0.6 to 0.7, which suggests that the He I line will contribute 60% to 70% of the Brγ intensity to the continuum level, in agreement with the empirically evaluated 61% level in § 2.3.1 and the 70% level in M16 (L00). Since Brγ emission is 7% of the Ks continuum, the He I contamination in the filter will be up to 4%, assuming the distribution is the same.

6. SUMMARY

We present the first and fully calibrated H_2 1–0 S(1) emission image of the entire 30 Doradus nebula, as well as a Brγ image. In the data reduction process, we confirmed Brγ and He I emission line contamination in the Ks continuum via empirical analysis and Cloudy simula-

Table 2
Emission lines within the Ks bandpass

Line	Wavelength
Brγ	$2.17\,\mu m$
He I 2 ^{1}P–2 ^{1}S	$2.06\,\mu m$
H_2 1–0 S(2)	$2.03\,\mu m$
H_2 1–0 S(1)	$2.12\,\mu m$
H_2 1–0 S(0)	$2.22\,\mu m$
H_2 2–1 S(1)	$2.25\,\mu m$

tions. The error in contamination-corrected H_2 images is estimated to be $\sim 4\%$.

The overall morphology of H_2 correlates well with Brγ and CO emission, implying that the observed H_2 originates from the PDRs in 30 Doradus. The brightest H_2-emitting areas (Area A and Area B) are PDRs viewed face-on located behind the ionizing source R136, and the warm molecular clouds traced by H_2 appear to be clumpy. Those regions also trace the CO morphology well, further indicating that these PDRs are face-on, with layers of ionized gas, warm molecular gas, and cold molecular clouds. Discontinuity of H_2 and Brγ morphology is found at the outer shells and pillar features (such as Area C) in 30 Dor , where the H_2 pillars are encompassed by Brγ envelops of sharp boundaries. This suggests that we are viewing the the shells and pillars of the H II region edge-on. The mean projected separation between the Brγ envelope and H_2 clumps is 3 pc ($A_V < 0.7$), indicating that H_2 emission is formed in the PDRs close to the surface of the molecular clouds. The density of H_2-emitting gas is inferred from the observed H_2-to-Brγ line ratios, the Cloudy model results, as well as theoretical predictions of H_2 emission in PDRs. The molecular gas density is estimated to be $< 10^4$ cm^{-3}. Low H_2-to-Brγ line ratios (< 0.5), as well as good morphological correlations between the H_2 and $8\,\mu m$ emission, implying again that the observed H_2 emission is excited by FUV radiation.

While it requires multiple transitions of ro-vibrational H_2 lines to constrain the excitation mechanisms and physical parameters of the ISM, such data do not yet exist. Our imaging observations suggest that the observed H_2 emission likely arises from a lower density layer of the PDR near IFs in 30 Doradus. We found no sign of shock-excited H_2 emission, and all indications were consistent with fluorescent excitation.

REFERENCES

Anderson, C. N., Meier, D. S., Ott, J., et al. 2014, ApJ, 793, 37

Bertin, E. & Arnouts, S. 1996, A&AS, 117, 393
Binette, L., Wilson, A. S., Raga, A., & Storchi-Bergmann, T. 1997, A&A, 327, 909
Black, J. H. & van Dishoeck, E. F. 1987, ApJ, 322, 412
Chu, Y.-H. & Kennicutt, Jr., R. C. 1994, ApJ, 425, 720
Conti, P. S. & Crowther, P. A. 2004, MNRAS, 355, 899
Crowther, P. A. & Dessart, L. 1998, MNRAS, 296, 622
Cyganowski, C. J., Whitney, B. A., Holden, E., et al. 2008, AJ, 136, 2391
Davis, C. J., Froebrich, D., Stanke, T., et al. 2009, A&A, 496, 153
de Koter, A., Heap, S. R., & Hubeny, I. 1998, ApJ, 509, 879
Dopita, M. A., Fischera, J., Crowley, O., et al. 2006, ApJ, 639, 788
Dopita, M. A., Groves, B. A., Fischera, J., et al. 2005, ApJ, 619, 755
Draine, B. T. 1978, ApJS, 36, 595
—. 2011, ApJ, 732, 100
Elmegreen, B. G. & Lada, C. J. 1977, ApJ, 214, 725
Fall, S. M., Krumholz, M. R., & Matzner, C. D. 2010, ApJ, 710, L142
Ferland, G. J., Korista, K. T., Verner, D. A., et al. 1998, PASP, 110, 761
Flower, D. R. & Pineau des Forêts, G. 2003, MNRAS, 343, 390
Habing, H. J. 1968, Bull. Astron. Inst. Netherlands, 19, 421
Hester, J. J., Scowen, P. A., Sankrit, R., et al. 1996, AJ, 111, 2349
Hillier, D. J. & Miller, D. L. 1998, ApJ, 496, 407
Indebetouw, R., Brogan, C., Chen, C.-H. R., et al. 2013, ApJ, 774, 73
Indebetouw, R., de Messières, G. E., Madden, S., et al. 2009, ApJ, 694, 84
Johansson, L. E. B., Greve, A., Booth, R. S., et al. 1998, A&A, 331, 857
Joseph, R. D., Wade, R., & Wright, G. S. 1984, Nature, 311, 132
Krumholz, M. R., Matzner, C. D., & McKee, C. F. 2006, ApJ, 653, 361
Lee, H.-T., Liao, W.-T., Froebrich, D., et al. 2013, ApJS, 208, 23
Leitherer, C., Schaerer, D., Goldader, J. D., et al. 1999, ApJS, 123, 3
Levenson, N. A., Graham, J. R., McLean, I. S., et al. 2000, ApJ, 533, L53
Maeder, A. & Meynet, G. 1994, A&A, 287, 803
Massey, P. & Hunter, D. A. 1998, ApJ, 493, 180
Matzner, C. D. 2002, ApJ, 566, 302
Medling, A. M., U, V., Rich, J. A., et al. 2015, MNRAS, 448, 2301
Micelotta, E. R., Jones, A. P., & Tielens, A. G. G. M. 2010, A&A, 510, A36
Moorwood, A. F. M. & Oliva, E. 1988, A&A, 203, 278
Murray, N., Quataert, E., & Thompson, T. A. 2010, ApJ, 709, 191
Oey, M. S., Watson, A. M., Kern, K., & Walth, G. L. 2005, AJ, 129, 393

Pauldrach, A. W. A., Hoffmann, T. L., & Lennon, M. 2001, A&A, 375, 161
Pellegrini, E. W., Baldwin, J. A., & Ferland, G. J. 2010, ApJS, 191, 160
—. 2011, ApJ, 738, 34
Persson, S. E., Murphy, D. C., Krzeminski, W., Roth, M., & Rieke, M. J. 1998, AJ, 116, 2475
Pineda, J. L., Mizuno, N., Röllig, M., et al. 2012, A&A, 544, A84
Pineda, J. L., Ott, J., Klein, U., et al. 2009, ApJ, 703, 736
Poglitsch, A., Krabbe, A., Madden, S. C., et al. 1995, ApJ, 454, 293
Probst, R. G., George, J. R., Daly, P. N., Don, K., & Ellis, M. 2008, in Society of Photo-Optical Instrumentation Engineers (SPIE) Conference Series, Vol. 7014, Society of Photo-Optical Instrumentation Engineers (SPIE) Conference Series
Puxley, P. J., Ramsay Howat, S. K., & Mountain, C. M. 2000, ApJ, 529, 224
Rahman, M., Moon, D.-S., & Matzner, C. D. 2011, ApJ, 743, L28
Riffel, R. A., Storchi-Bergmann, T., & Nagar, N. M. 2010, MNRAS, 404, 166
Rodríguez-Ardila, A., Pastoriza, M. G., Viegas, S., Sigut, T. A. A., & Pradhan, A. K. 2004, A&A, 425, 457
Rodríguez-Ardila, A., Riffel, R., & Pastoriza, M. G. 2005, MNRAS, 364, 1041
Rubio, M., Barbá, R. H., Walborn, N. R., et al. 1998, AJ, 116, 1708
Smith, L. J., Norris, R. P. F., & Crowther, P. A. 2002, MNRAS, 337, 1309
Sternberg, A. & Dalgarno, A. 1989, ApJ, 338, 197
Swaters, R. A., Valdes, F., & Dickinson, M. E. 2009, in Astronomical Society of the Pacific Conference Series, Vol. 411, Astronomical Data Analysis Software and Systems XVIII, ed. D. A. Bohlender, D. Durand, & P. Dowler, 506
Townsley, L. K., Broos, P. S., Feigelson, E. D., et al. 2006, AJ, 131, 2140
Turner, J., Kirby-Docken, K., & Dalgarno, A. 1977, ApJS, 35, 281
van Dishoeck, E. F. & Black, J. H. 1988, ApJ, 334, 771
Verdolini, S., Yeh, S. C. C., Krumholz, M. R., Matzner, C. D., & Tielens, A. G. G. M. 2013, ApJ, 769, 12
Weingartner, J. C. & Draine, B. T. 2001, ApJ, 548, 296
Whitworth, A. 1979, MNRAS, 186, 59
Williams, J. P. & McKee, C. F. 1997, ApJ, 476, 166
Wolniewicz, L., Simbotin, I., & Dalgarno, A. 1998, ApJS, 115, 293
Wong, T., Hughes, A., Ott, J., et al. 2011, ApJS, 197, 16
Yeh, S. C. C. & Matzner, C. D. 2012, ApJ, 757, 108
Yeh, S. C. C., Verdolini, S., Krumholz, M. R., Matzner, C. D., & Tielens, A. G. G. M. 2013, ApJ, 769, 11
Zavagno, A., Anderson, L. D., Russeil, D., et al. 2010, A&A, 518, L101